Publication III

Arttu Polojärvi, Jukka Tuhkuri and Otto Korkalo. Comparison and analysis of experimental and virtual laboratory scale punch through tests. ***Cold Regions Science and Technology*****, 81, 11-25, 2012.**

Cold Regions Science and Technology 81 (2012) 11–25

Contents lists available at SciVerse ScienceDirect

Cold Regions Science and Technology

journal homepage: www.elsevier.com/locate/coldregions

Comparison and analysis of experimental and virtual laboratory scale punch through tests

Arttu Polojärvi [a,*], Jukka Tuhkuri [a], Otto Korkalo [b]

[a] Aalto University, School of Engineering, Department of Applied Mechanics, P.O. Box 14300, FI-00076 Aalto, Finland
[b] VTT Technical Research Centre of Finland, P.O. Box 1000, FI-02044 VTT, Finland

ARTICLE INFO

Article history:
Received 4 January 2012
Accepted 26 April 2012

Keywords:
Ice rubble
Numerical modelling
Discrete element method
Punch through tests
Model scale experiments

ABSTRACT

Laboratory scale punch through tests on floating rubble consisting of plastic blocks were conducted and simulated with a 3D discrete numerical model. The purpose was to analyse the experimental method and to validate the model. The motivation of using plastic blocks instead of ice was to simplify the interpretation of results as the plastic blocks do not freeze together. The indentor force and the lateral force induced by the rubble on one of the basin walls were recorded as a function of indentor penetration. Further, the experiments were recorded with a video camera and a motion tracking software was used to analyse the rubble deformation. The force records and deformation patterns from the experiments and simulations were in agreement. The evolution of the deformation patterns could be closely linked to the indentor force records, which demonstrates the need for the numerical model to correctly represent the rubble deformation. The experiments and the simulations showed, that the lateral force within the pile increased considerably during a punch through experiment. This makes the interpretation of punch through experiment results for material modelling challenging: the friction angle of the rubble can become overestimated making the punch through test unsuitable for achieving accurate values for friction angle. Consequently, no value for the rubble friction angle was derived here.

1. Introduction

Punch through experiments are an important method for testing ice rubble properties. In a punch through experiment, a flat indentor platen penetrates through the rubble mass while the force applied by the rubble on the indentor is measured. From the indentor force-displacement records and the dimensions of the experimental set up, some rubble properties can be derived.

First punch through experiments were performed by Leppäranta and Hakala (1992) in the Baltic Sea using a loading platform and concrete blocks. Since then, the experimental equipment has been improved and the method has been used in full scale as reported in e.g. Bruneau et al. (1998), Heinonen and Määttänen (2000, 2001a, b), Croasdale et al. (2001) and Heinonen (2004). Even if efforts have been made to measure and visually observe the rubble deformation in full scale experiments (Croasdale et al., 2001; Heinonen, 2004), the possibilities to study the actual failure mechanisms of the ice rubble have been rather limited.

On the other hand, the knowledge on the failure mechanism of the rubble is of crucial importance in the development of material models for the ice rubble. For the more detailed analysis on the behaviour and failure mechanism of rubble, laboratory scale punch through experiments have been performed by e.g. Leppäranta and Hakala (1992), Bruneau et al. (1998), Azarnejad et al. (1999), Azarnejad and Brown (2001), Jensen et al. (2001), Lemee and Brown (2002), and Serré (2011).

While the results from the laboratory scale experiments have increased the understanding on the failure of a rubble, they have also yielded results that differ from those achieved in the field (Croasdale et al., 2001; Liferov and Bonnemaire, 2005). One of these differences is the loading rate dependency of the rubble behaviour first found in laboratory experiments by Azarnejad and Brown (2001). The loading rate dependency has been earlier discussed in a review by Liferov and Bonnemaire (2005) and analysed in Polojärvi and Tuhkuri (2012).

Another important difference is that in the laboratory the indentor displacements at maximum loads are relatively high when compared to those in the full scale. This is believed to indicate difference in rubble behaviour between laboratory and full scale experiments. In full scale, the maximum loads are believed to be dominated by the failure load of the cohesive skeleton formed by freeze bonds (Heinonen, 2004; Liferov and Bonnemaire, 2005). Further, it has been assumed that it is only after the breakage of this skeleton that the frictional resistance of the pile becomes mobilized. In the laboratory, the rubble usually goes through considerable deformation before maximum indentor force is reached and it is believed that also the frictional resistance contributes significantly to the maximum load (Liferov and Bonnemaire, 2005).

* Corresponding author. Tel.: +358 9 470 23438.
E-mail address: arttu.polojarvi@aalto.fi (A. Polojärvi).

0165-232X/$ – see front matter © 2012 Elsevier B.V. All rights reserved.
doi:10.1016/j.coldregions.2012.04.008

This latter difference motivates the punch through experiments on non cohesive rubble presented in this paper. In this work, laboratory scale punch through experiments were performed using rubble consisting of plastic blocks. The motivation of using plastic blocks instead of ice blocks was to simplify the interpretation and analysis of the results. When plastic blocks are used, freeze bonds between the blocks and other features, e.g. sintering, characteristic to the ice rubble are avoided (Ettema and Schaefer, 1986; Kuroiwa, 1961).

The understanding on failure mechanisms is also important for the modelling efforts of the ice rubble. The modelling of granular material such as rubble is challenging. Earlier work in modelling of ice rubble has included analytic soil mechanics models (Ettema and Urroz, 1989), continuum models (Heinonen, 2004; Heinonen and Määttänen, 2001b; Liferov et al., 2002, 2003; Serré, 2011), discrete models (Polojärvi and Tuhkuri, 2009; Tuhkuri and Polojärvi, 2005) and pseudo-discrete models (Liferov, 2005).

In the work presented in this paper, rubble pile was numerically modelled as 3D discontinuous media. In this type of modelling, the rubble consists of individual blocks which interact through contacts. Further, the deformation of the rubble is due to displacements of the blocks within it. Two techniques commonly used in numerical modelling of discontinuous media are the discrete element method (DEM) and combined finite–discrete element method (FEM–DEM), first introduced by Cundall and Strack (1979) and Munjiza et al. (1995), respectively. In ice mechanics, DEM and FEM–DEM have earlier been used e.g. in studies of ice ridging (Hopkins, 1992, 1998; Hopkins et al., 1999), ice pile-up against structures (Haase et al., 2010; Paavilainen and Tuhkuri, 2012; Paavilainen et al., 2006, 2009, 2011) and punch through experiments (Polojärvi and Tuhkuri, 2009, 2010; Tuhkuri and Polojärvi, 2005).

Here, the individual blocks within the simulated rubble were assumed rigid. The contact forces between the blocks were solved using penalty functions and potential contact force method (Munjiza, 2004). This modelling technique for contact forces was chosen as it gives robust platform for solving 3D contacts of polyhedral blocks.

The purpose of this paper is two-fold. First the experimental results are presented and compared to the results from the numerical model. Through the comparison the model is validated and its applicability to simulate ice mechanics related problems thus demonstrated. Then the experimental and modelling results are analysed in parallel. The scope of the analysis is to gain further understanding on the failure process of the rubble and to briefly discuss the implications of the results to the material modelling of the rubble. No rubble material properties apart from the rubble shear strength are derived using the results.

The article is organized as follows. First the experimental set up and the results from the experiments are presented in Section 2. Then, the numerical modelling of the experiments is introduced in Section 3. After this in Section 4, the results from the experiments and the simulations are presented, compared and analysed. The implications of the results on the interpretation of punch through experiment results and on the material modelling of the rubble results are briefly discussed in Section 5. Finally, the conclusions are presented in Section 6.

2. Experiments

In this section, the experimental set up and the conducted experiment types are described. Then a run through of punch through experiments is presented with a description of indentor load records. In the end of the section, the derivation of the load records due to rubble material is presented. The experimental set up is here described only briefly, but more data on it can be found from Polojärvi and Tuhkuri (2012).

2.1. Experimental set up

The test basin illustrated in Fig. 1 was made of transparent acrylic glass (PMMA) and was supported by a steel frame. The basin dimensions were $2.5\times0.5\times1.0$ m. The indentor platen was $0.5\times0.49\times0.01$ m and made of polyethylene (PE). The basin had movable PE walls attached to the basin frame which enabled to change its width w_b. The lateral force F_x applied by the rubble on the instrumented movable wall at $x=-w_b/2$ was measured to investigate the lateral confinement within the rubble. In some of the experiments, covers were installed into the basin. The covers were cut from a 0.01 m thick PE plate and reached from the edges of the indentor platen to the movable walls.

The main properties of the rubble blocks are given in Table 1. The blocks had a shape of a rectangular cuboid and were sawn out of 0.02 m thick PE plate by the supplier. The PE plate unfortunately had different surface roughness on its opposing faces, hence the surface roughness on opposing block faces differed. The sliding friction coefficient μ for wet blocks was measured as described in Polojärvi and Tuhkuri (2012). Value of μ depended on the pair of contacting block faces and varied between 0.04 and 0.12.

2.2. Experiment types

The summary of the tests reported in this paper is given in Table 2. As the table shows, two different types of punch through experiments were conducted: uncovered and covered basin experiments. The experiment types differed by the boundary conditions on the top of the rubble. In the covered basin experiments, the rubble besides the indentor platen was covered by PE-plates whereas in the uncovered basin experiments these plates were not used. In addition to actual punch through tests, open water experiments with no rubble in the

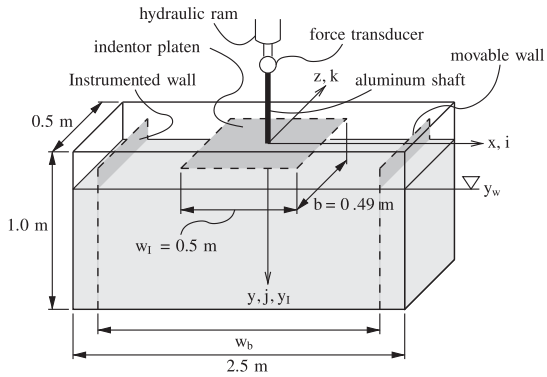

Fig. 1. Experimental set up. Direction of the indentor motion y_I is indicated. The coordinate system (x,y,z) has its origin in the indentor centroid in its initial position. Further, the water surface y_w is shown (water shown in gray). The lateral force was measured on the instrumented wall at $x=-w_b/2$. The instrumented wall was also movable even if not indicated in the figure. The rubble and the basin covers are not shown in the figure for clarity.

Table 1
Properties of the rubble blocks.

Property	Symbol	Unit	Value
Length	–	m	0.09
Width	–	m	0.05
Thickness	–	m	0.02
Material density	ρ	kg m^{-3}	949 ± 7.8
Friction coefficient	μ	–	0.04…0.12

Table 2
Summary of the testing program: the number of conducted experiments with both basin widths w_b and indentor velocities v_I, and with all rubble thicknesses h. In the table, N.A. stands for not applicable.

Test type	w_b [m]	h [m]	Number of experiments	
			$v_I = 2.5$ mm/s	$v_I = 5$ mm/s
Punch through	1.5	0.3	4	4
		0.4	4	4
		0.5	4	4
	2.3	0.3	5	5
		0.4	5	5
		0.5	5	5
Covered basin	1.5	0.3	1	1
		0.4	2	2
		0.5	6	6
	2.3	0.3	5	3
		0.4	2	3
		0.5	4	3
Open water	2.3	N.A	3	3

basin were conducted for taking account the contribution of the experimental equipment to the measured load records. Both types of punch through experiments were conducted with two basin widths w_b to study the potential effect of w_b on force records and deformation patterns of the rubble.

Albeit idealized, the boundary conditions in the experiments are comparable to those in the punch through experiments with ice rubble. The boundary conditions in the experiments performed on ice rubble with no freeze bonds are similar to those of uncovered experiments. Instead, in a punch through experiment on ice rubble with freeze bonds, a layer of ice (ice sheet or consolidated layer) initially covers the rubble. To conduct an experiment on the rubble only, this layer is typically cut along indentor platen perimeter (Azarnejad and Brown, 2001; Heinonen, 2004; Serré, 2011). This procedure leads to boundary conditions similar to those in the covered basin experiments here.

Before each punch through experiment, the rubble pile was first mixed to ensure its random initial configuration. After this, in a covered basin experiment, the covers were installed into the basin with their lower face below the water line. Further, the indentor was carefully lowered on top of the rubble to avoid blocks from getting jammed between the moving indentor and the covers in the actual experiment. In an uncovered basin experiment, the rubble was left as it was after the mixing, and the indentor started its motion above the rubble.

Indentor velocities 2.5 mm/s and 5 mm/s were used in the experiments. The indentor velocity during its penetration remained virtually constant (Polojärvi and Tuhkuri, 2012). The relatively slow indentor velocities used here enabled factoring the measured indentor load into the contribution of the experimental set up and the contribution due to rubble material. The factoring was performed using the results from the open water experiments as shown below. With high indentor velocities, this type of factoring becomes challenging as shown in Polojärvi and Tuhkuri (2012). The indentor velocities were not chosen after any full scale ice rubble processes, but to study the experimental method and ice rubble behaviour in quasi static punch through experiments and to validate the numerical model which did not include hydrodynamical forces besides a simple model for block drag.

2.3. Indentor and rubble force records from the experiments

The experiments were found to be well repeatable, thus the indentor force F_I records from the repeated experiments were used to derive the mean indentor force $\bar{F}_I$ records as presented in Polojärvi and Tuhkuri (2012). Typical $\bar{F}_I$ records from both punch through experiment types are shown in Fig. 2a and b. As seen from the figures, experiments with both basin widths w_b yielded to very similar $\bar{F}_I$ records.

In both experiment types, $\bar{F}_I$ first started to increase in the beginning of the experiment as shown in Fig. 2a and b. The rate $\partial\bar{F}_I/\partial y_I$ then changed due to the indentor platen buoyancy as the platen started its water entry. Further, all $\bar{F}_I$ records show a local peak which always occurred after the indentor submergence and was related to hydrodynamics (Polojärvi and Tuhkuri, 2012). After the peak, $\bar{F}_I$ corresponded to the rubble resistance and to the combined load of the rubble and the indentor platen buoyancies. In the uncovered basin experiments, $\bar{F}_I$ decreased after the peak until the end of the experiment. Instead, in the covered basin experiments, $\bar{F}_I$ still increased after the peak and started to decrease later in the experiment.

The F_I records from the punch through and the open water experiments were used to derive load records due to rubble material for the analysis presented in Section 4. As illustrated in Fig. 3a and b, the rubble load F_R records were derived by subtracting F_I records from the open water experiments from those from the punch through experiments. The derivation of F_R records by subtraction was applicable, as F_I records from the open water and the punch through experiments showed similar features: the rate $\partial\bar{F}_I/\partial y_I$ during the indentor platen water entry in them was approximately equal and they both showed

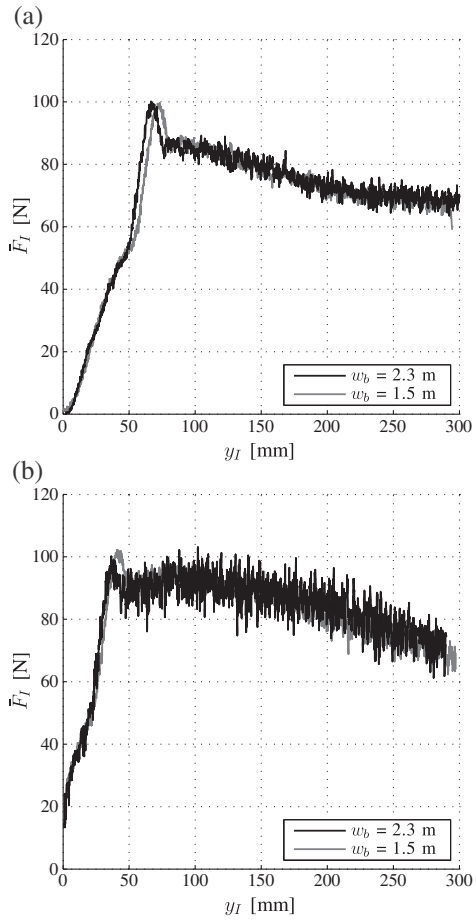

Fig. 2. Mean indentor force $\bar{F}_I$ records from punch through experiments with $v_I = 5$ mm/s, $h = 0.5$ m, and with both basin widths w_b: (a) uncovered and (b) covered basin experiments.

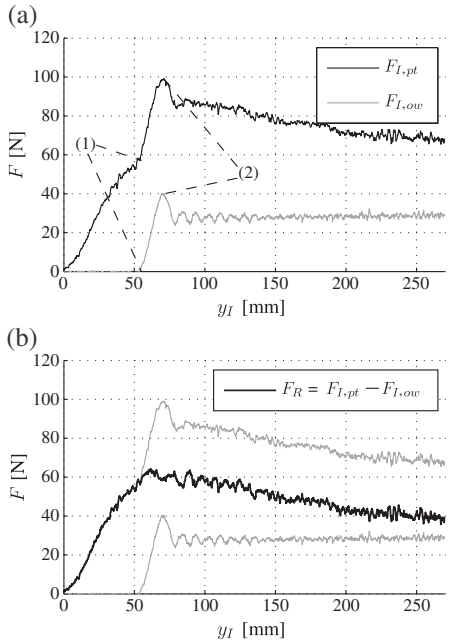

Fig. 3. The derivation of the rubble load F_R: (a) indentor load records from a punch through ($F_{I,pt}$) and an open water ($F_{I,ow}$) experiment and (b) the rubble load $F_R = F_{I,pt} - F_{I,ow}$. In (a), the indentor starts its entry into the water at (1) and the peak related to the hydrodynamic force occurs at (2) after the indentor submergence (Polojärvi and Tuhkuri, 2012). The data from the open water experiment is shifted right so that the indentor position in relation to the water surface in both experiments is equal. In (b), $F_{I,pt}$ and $F_{I,ow}$ from (a) are shown in gray.

a local peak. This local peak was due to hydrodynamics after the platen submergence as presented in more detail in Polojärvi and Tuhkuri (2012).

As the example in Fig. 3 illustrates, the rubble load F_R records showed no distinct peak force. The lack of peak force indicates, that the rubble resistance was due to the rubble buoyancy and friction: in the case of a sudden failure of a cohesive network, a peak followed by a drop in F_R would be expected. As the F_I records from the repeated experiments were similar, the F_R records derived from them were also similar. Therefore, the F_R records from the repeated experiments could be used to derive mean rubble load $\bar{F}_R$ records used in the further text.

3. Simulations of experiments

In the discrete numerical model used here, the rubble pile consisted of numerous individual rigid blocks interacting through contacts. In addition to forces due to contacts, the block forces were due to buoyancy, gravitation and water drag. All forces applied on blocks were determined as presented in Appendix A. The simulations were run in 3D in a domain with dimensions of the basin used in the experiments (see Fig. 1). The basin walls in the simulations were rigid and were not allowed to move.

The simulations were performed in two phases: (1) in the initial phase the initial configuration of the rubble was generated and (2) in the punch through phase the indentor platen penetrated the rubble. In the first phase, the initial configuration of the pile was generated by releasing blocks under water with random orientations and velocities. After releasing, the blocks were allowed to float until their kinetic energy was dissipated due to friction, drag and damping in contacts and a quasi static pile had formed. In the covered basin simulations, the covers and the indentor were lowered on top of the quasi static rubble pile in the end of the initial phase.

Typical rubble piles at the beginning of punch through phase of the simulations are illustrated in Fig. 4a and b. In the punch through phase, the indentor penetrated into the rubble with constant indentor velocity. During the penetration, the force applied on the indentor platen and on basin walls due to rubble blocks was gauged. The hydrodynamics, besides the simplified drag force acting on rubble blocks, were not modelled. Hence, the indentor load records from the punch through phase of the simulations could be directly compared to the experimental F_R records (see Fig. 3).

The main parameters for the simulations presented in the next section are given in Table 3. The block shape, size and mass properties in the simulations were chosen after the experiments. As mentioned above, the friction coefficient μ in the experiments depended on the pair of contacting block faces: in the simulations $\mu = 0.08$, chosen after the mean value of friction coefficients measured in the experiments, was used. Reference simulations with friction coefficient depending on the pair of contacting faces were performed with no change in results presented below. This shows, that the number of contacting faces was high enough to make the effect of varying friction coefficient to disappear. The drag coefficient in the simulations had value $C_d = 1.05$ chosen after a shape of a cube (Granger, 1995). The bulk porosity η given in the table is defined as $\eta = (V_r - V_b)/V_r$, where V_r and V_b are the volume of rubble and the volume of blocks within the rubble, respectively. V_b was readily available in the simulations and V_r was determined by post processing the simulation data.

The results in the next section are from simulations with indentor velocity $v_I = 10$ mm/s. The results from the simulations are compared to the experiments with $v_I = 2.5$ mm/s and 5 mm/s. The comparison of the results from the simulations and the experiments with

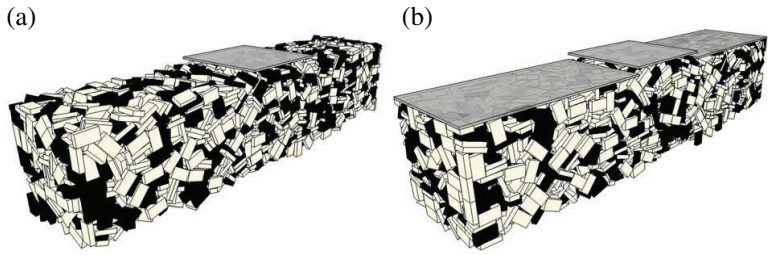

Fig. 4. Examples of typical initial rubble configurations before indentor penetration in simulated punch through experiment: simulation of (a) an uncovered and (b) a covered basin experiment. The basin walls are not shown in the figure for clarity.

Table 3
Main parameters used in simulations presented in Section 4. Details of the numerical model are given in Appendix A. The directions (Dir.) given in the table refer to the global coordinate system in Fig. 1. Basin covers reached from the indentor edges ($x = \pm w_I/2$) to basin walls ($x = \pm w_b/2$) in x-direction (see Fig. 4b), hence their width depended on basin width and is not given in the table.

	Parameter	Dir.	Symbol	Unit	Value
General	Number of blocks	–	–	–	1450…3800
	Gravitational acceleration	–	g	ms^{-2}	9.81
Contact	Penalty term	–	s	–	$1 \cdot 10^6$
	Damping constant	–	c	$Ns\,m^{-3}$	$1 \cdot 10^5$
	Time step	–	Δt	s	$5 \cdot 10^{-5}$
Blocks	Length	–	–	m	0.09
	Width	–	–	m	0.05
	Thickness	–	–	m	0.02
	Mass density	–	ρ_b	$kg\,m^{-3}$	949
	Friction coefficient	–	μ	–	0.08[a]
	Drag coefficient	–	C_d	–	1.05
Water	Mass density	–	ρ_w	$kg\,m^{-3}$	1000
Rubble	Keel depth	–	h	m	0.3,0.4,0.5
	Bulk porosity	–	η	–	~0.4
Indentor	Width	x	w_I	m	0.5
	Length	z	–	m	0.49
	Thickness	y	–	m	0.01
	Velocity	y	v_I	$mm\,s^{-1}$	10
	Stroke length	y	–	m	0.3
Covers	Length	z	–	m	0.5
	Thickness	y	–	m	0.01
Basin	Width	x	w_b	m	1.5,2.3
	Length	z	–	m	0.5

[a] Same friction coefficient was used for block–block and block–wall contacts.

different values of v_I was applicable, as additional simulations with $v_I = 5$ mm/s showed negligible change in results. The indentor load histories from these additional simulations are presented in Appendix B. Limited use of low v_I values was related to the length of the simulation times: the decrease in v_I leads to an increase in simulated time period and thus to an increase in simulation time.

4. Results, model validation and analysis

4.1. Comparison of rubble load records

As mentioned above, the rubble load F_R records derived from indentor load records (see Fig. 3) could be directly compared to the indentor load records from the simulations. Therefore, the experimental F_R records and indentor load records from the simulations are both referred to with the same symbol F_R below. The repeated simulations with different initial rubble configurations yielded to similar F_R records and were used to derive mean load records, which are referred to with symbol $\bar{F}_R$ similarly to the experimental mean rubble load records.

The load records and levels in the simulations and experiments were in good agreement as illustrated by Figs. 5 and 6. The $\bar{F}_R$ records shown in Fig. 5a and b from the experiments and simulations are similar: in both F_R increased with the same rate in the beginning of the indentor penetration and reached its maximum with approximately equal indentor displacement. In the covered basin simulations $\bar{F}_R$ was underestimated towards the end of the indentor stroke, whereas in the uncovered simulations $\bar{F}_R$ records were in good agreement until the end of the experiment. The maximum rubble load $\bar{F}_R^m$ values were also approximately equal in experiments and simulations as shown by Fig. 6a and b. The basin width w_b had no major effect on F_R records nor F_R^m values as further shown by Figs. 5 and 6.

As illustrated by Fig. 5a and b, in both experiments and simulations, the indentor displacement as F_R^m was reached depended on the experiment type. When the basin was uncovered, F_R^m was reached close to the indentor submergence, but when the basin was covered,

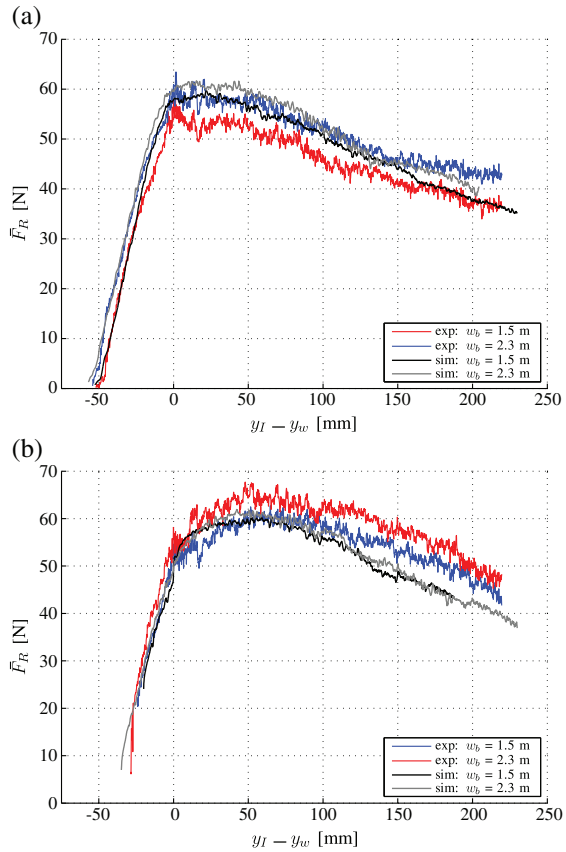

Fig. 5. The mean rubble load $\bar{F}_R$ records from the experiments and the simulations: (a) uncovered and (b) covered basin. $\bar{F}_R$ records from the experiments and simulations with rubble thickness 0.5 m and both basin widths w_b are shown. The x-axis shows the indentor position in relation to the water surface y_w.

F_R was in general still increasing at indentor submergence and F_R^m was reached later in the experiment. The reason for this behaviour was a difference in the evolution of the rubble deformation patterns between experiment types, as shown in the next section.

4.2. Deformation of the rubble

In addition to load records, the deformation patterns in the simulations and experiments were found to be in good agreement as presented below. Further, the evolution of the deformation patterns and the mass flow of the rubble material appear to have a close relation with the rubble load F_R records. This demonstrates the need for a numerical model to correctly represent mass flow of the rubble.

4.2.1. Visualization of the deformation patterns

The visual analysis on the rubble deformation in the experiments was based on the video recordings. The recordings were post processed using a motion tracking software which detected and tracked the block corners throughout the experiment giving their trajectories. The trajectories were then used in the analysis on deformation patterns as follows.

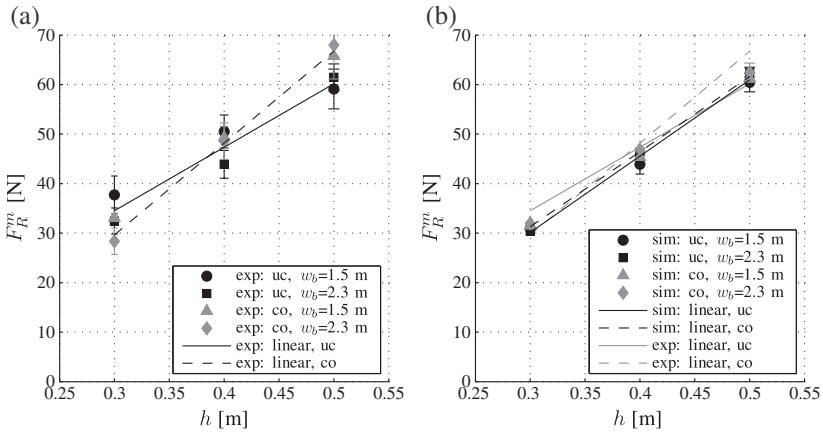

Fig. 6. Mean values of maximum rubble load F_R^m with their standard deviations in (a) uncovered (un) and covered (co) basin experiments and in (b) corresponding simulations. The linear fits in the figures for different experiment typesinclude data from experiments and simulations with both w_b. The data in (a) is from experiments with indentor velocities 2.5 mm/s and 5 mm/s and in (b) from the simulations with $v_I = 10$ mm/s.

For each block corner j, its coordinate $\mathbf{x}_j^k = \{x_j^k, y_j^k\}$ (coordinate system given in Fig. 1) at the time instant of frame k of the recording was first used to derive displacement of the corner from

$$\Delta\mathbf{x}_j^k = \Delta x_j^k\mathbf{i} + \Delta y_j^k\mathbf{j} = \left(x_j^k - x_j^0\right)\mathbf{i} + \left(y_j^k - y_j^0\right)\mathbf{j}, \quad (1)$$

where x_j^0 and y_j^0 are the corner coordinates in the initial rubble configuration.

These displacements were then used to estimate displacing rubble volume as illustrated in Fig. 7a and b. First, the indentor displacement y_I^k for frame k was determined. Then, tracking points with $y_j^k > Ry_I^k$, where R is a constant, were picked from the data (Fig. 7a). After this, the points with $\Delta y_j^k > Ry_I^k$ were used to define a convex hull (Fig. 7b). The area of the hull was used to estimate the volume of rubble with $\Delta y_j^k > Ry_I^k$. By varying R, a presentation for the deformation pattern of the rubble was achieved.

The trajectories of the block corners in the simulations were achieved in similar manner by post processing the simulation data in MATLAB (MATLAB, 2009). As the analysis based on the video in the experiments was limited to the visible part of the rubble, only the block vertices within the distance of block length (0.09 m) from the long basin wall at $z = -0.25$ m (see Fig. 1) were used when analysing the data from the simulations.

4.2.2. Comparison of the deformation patterns in experiments and simulations

Snapshots in Fig. 8 illustrate rubble deformation during covered basin punch through experiments and corresponding simulations. In the snapshots of Fig. 8, hulls for the rubble volumes with $\Delta y_j^k > Ry_I$, $R = 0.90$, 0.75, 0.50 and 0.10 are superposed on top of the images from experiments and simulations. The hull with the highest R value (0.90) estimates the volume of rubble moving with the indentor, whereas the hull with the smallest R (0.10) gives an approximation for the total volume of the downwards moving rubble mass.

The first snapshot in Fig. 8 with $y_I = 35$ mm shows the rubble at the point, where indentor platen has reached the water surface. The rubble mass under the indentor is observed to move with the platen (hulls with $R > 0.90$ in the figure). The volume of this mass has an approximate shape of a wedge with one corner reaching downwards into the y-direction and one side aligning with the indentor platen. The corner reaching downwards stayed within the indentor edges in x-direction.

The next snapshot in Fig. 8 with $y_I = 80$ mm shows the deformation patterns at the maximum rubble load F_R^m. The volume of displaced rubble has increased from the previous snapshot, whereas the volume of the rubble moving with the indentor ($R > 0.90$) is observed to have stayed similar. The increase in the volume of the hulls with $R < 0.90$ was due to increase in their width.

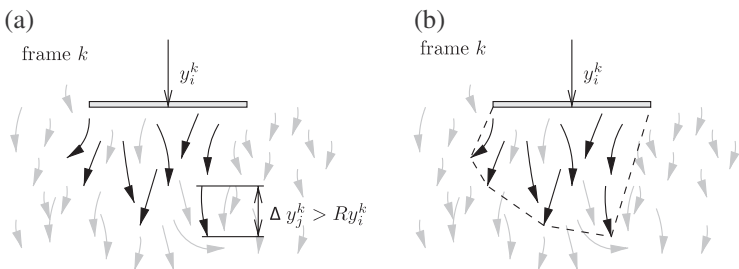

Fig. 7. Illustration of the technique for analysing deformation patterns of the rubble using video recording: (a) trajectories (arrows) of tracking points with $\Delta y_j^k > Ry_I^k$, where R is a constant, shown in black and (b) a convex hull including trajectories with $\Delta y_j^k > Ry_I^k$ (shown with dashed line) used in estimation of the displaced rubble volume.

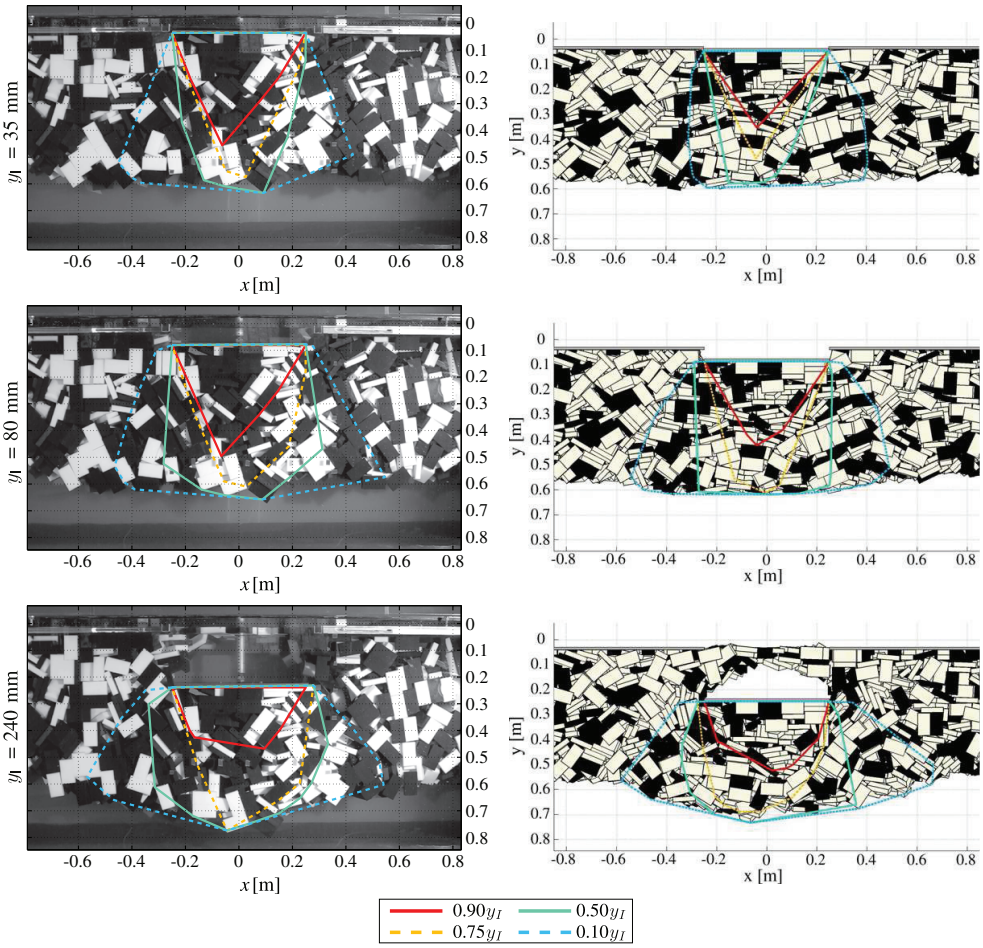

Fig. 8. The deformation patterns with increasing indentor displacement y_I in a covered basin experiment (left) and a corresponding simulation (right). The displacement values Ry_I for the hulls shown are given in the legend. The rubble thickness h and the basin width w_b were 0.5 m and 2.3 m, respectively, in the experiments and simulations shown. The indentor velocity v_I was 5 mm/s in the experiments and 10 mm/s in the simulations.

The last snapshot in Fig. 8 with $y_I = 240$ mm taken towards the end of the indentor stroke still shows that the deformation patterns are similar in the simulations and experiments. Lateral movement of the rubble towards the indentor center line above the indentor platen is observed.

4.2.3. Relation of deformation patterns and F_R records

The simulation data was used to analyse the relation between the F_R and rubble deformation in more detail as the analysis was not limited only on the visible part of the rubble. The displacing rubble volume during simulated experiments is again illustrated by Fig. 9a and b using the velocities of the blocks. The figures show the total volume of blocks with their centroids having the downward velocities $v_y > 2$ mm/s, $v_y > 5$ mm/s, and $v_y > 9$ mm/s in simulations with indentor velocity $v_I = 10$ mm/s. The basin width w_b did not affect these volumes, thus the data from the simulations with both w_b is included in the data shown in the figures.

Fig. 9 shows two distinct features: the experiment type has an effect on the evolution of the displacing rubble volumes and that the volume of displacing rubble is at its maximum close to the maximum rubble load F_R^m. The latter feature can be seen by comparison of F_R records in Fig. 5a and b to Fig. 9a and b: the maximas for the rubble volumes with $v_y > 5$ mm/s and $v_y > 9$ mm/s are reached approximately simultaneously with F_R^m. As a consequence of downwards moving rubble volume increasing during longer displacement interval in the covered than in the uncovered basin experiments, the maximum rubble load F_R^m is reached later in covered experiments.

As Fig. 9 further shows, the volume of solid material moving downwards decreased in all simulations towards the end of the indentor stroke. The main reason for this decrease was the movement of the blocks above the indentor platen illustrated by Fig. 10a and b, which show block centroid velocities into lateral and vertical directions towards the end of a simulated experiment. Fig. 10a clearly shows blocks above the indentor platen moving towards the indentor center line resulting into upward movement of rubble blocks through pile thickness seen in Fig. 10b.

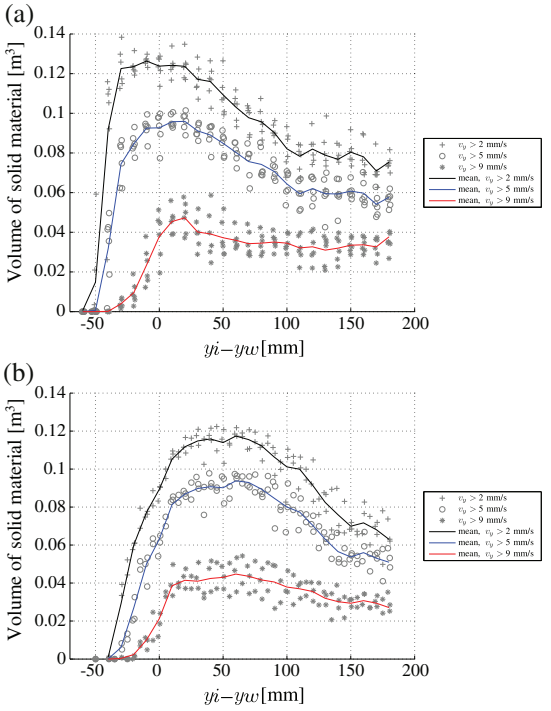

Fig. 9. The volumes of blocks moving downwards in simulated experiments with velocities $v_y = 9$, 5, and 2 mm/s: (a) uncovered and (b) covered basin simulations. The x-axis shows the indentor position y_I in relation to the water line y_w. In all simulations rubble thickness $h = 0.5$ m and indentor velocity $v_I = 10$ mm/s. Data from simulations with both basin widths is included in the figures.

4.3. Confining forces within the rubble

The lateral force F_x applied by the rubble on the instrumented wall of the basin was measured as described in Section 2. In the simulations, F_x was similarly to the experiments gauged on the short walls of the basin. As first shown below, F_x records from the experiments and simulations were in fair agreement. Further it is shown, that F_x was not constant, but first increased, during the indentor stroke. This indicates that the confining pressure within the pile increases during indentor penetration. The increase in F_x from its initial value was considerable and led to maximum lateral force values, F_x^m, which were relatively high in comparison to the vertical rubble load.

4.3.1. Lateral force records

Fig. 11 shows the mean lateral force $\bar{F}_x$ records from the covered basin experiments and simulations. Clearly, the lateral force F_x was not constant during the indentor stroke: first $\bar{F}_x$ increased and further reached a maximum, and then decreased until the end of the stroke. The $\bar{F}_x$ records unexpectedly differed in the beginning of the indentor penetration in the experiments with different basin widths w_b. The reason for this behaviour is unclear. The figure further shows, that the $\bar{F}_x$ records from the experiments and the simulations were similar excluding the unexpected discrepancy with the change in w_b in the beginning of the indentor motion.

To study the increase in F_x during experiments and simulations, the initial lateral force F_x^0 induced by the rubble before any indentor penetration, is first briefly discussed. Mean values of F_x^0 from covered basin experiments and simulations of both experiment types are given in Fig. 12a and b, respectively. As shown, F_x^0 increased with rubble thickness h as expected, with the simulations yielding slightly higher F_x^0 values than the experiments.

Fig. 13 shows the mean values of maximum lateral force F_x^m. The basin width w_b is observed to have an effect on F_x^m values in covered basin experiments with the rate $\partial F_x^m/\partial h$ being equal for both w_b. The comparison of Fig. 13a and b shows, that the simulations yielded to F_x^m values on the range of those in the experiments but F_x^m values were not affected by w_b. Further, as Fig. 11 and the comparison of Figs. 12 and 13 shows, the increase in F_x during indentor stroke was clear: with basin width $w_b = 1.5$ m ($w_b = 2.3$ m), F_x increased on average 63% (51%).

The values of F_x^m given in Fig. 13 were considerable in relation to the maximum rubble load F_R^m. This is illustrated by F_x^m/F_R^m ratios shown in Fig. 14a and b. Fig. 14 a shows, that F_x^m/F_R^m increased with h with F_x^m having values up to ~25% of F_R^m with $h = 0.5$ m in the covered basin experiments. The F_x^m/F_R^m ratios in the simulations were in general somewhat higher than in the experiments, as seen by comparison of Fig. 14a and b. This is especially clear for simulations with $h = 0.3$ m and $w_b = 2.3$ m, which yielded higher values of F_x^m than the corresponding experiments. With $h = 0.5$ m, F_x^m/F_R^m ratios from the simulations and experiments were in fair agreement.

4.3.2. Displacements at maximum lateral force

The indentor displacement y_x^m at maximum lateral force F_x^m was in general higher than indentor displacement y_R^m at maximum rubble load F_R^m in both simulations and experiments. This is illustrated by Fig. 15a and b, which shows values of $y_x^m - y_w$, where y_w is the water level, plotted against values of $y_R^m - y_w$. As the figures show, the majority of the data points have $y_x^m - y_R^m$ indicating that F_x^m was reached after F_R^m. Considering $\bar{F}_x$ records in Fig. 11 this indicates that F_x was generally increasing as F_R^m was reached. This has implications to the material modelling as briefly discussed next.

5. Discussion

5.1. Effect of the basin walls

The effect of basin walls on the experimental results in previous section was studied using the simulations. For this, the vertical frictional forces F_μ on rubble due to the basin walls were monitored in the simulations. Same friction coefficient value ($\mu = 0.08$) was used for block–wall and block–block contacts (see Table 3). The results below show, that the long basin walls (at $z = \pm 0.25$ m in Fig. 1) somewhat increased the maximum rubble load (F_R^m), and that the basin likely was wide enough for the short walls (at $x = \pm w_b/2$) to not affect the results presented above.

Typical F_μ records from simulations of both experiment types are given in Fig. 16a and b. In the figure, negative (positive) F_μ values indicate a wall resisting downwards (upwards) rubble movement. Hence, the friction at long walls of the basin resisted downwards rubble movement, whereas at the short walls, the upward rubble movement was resisted by friction.

Further Fig. 16a and b illustrates how the covers affected the F_μ records at the long walls: the maximum absolute value of frictional force in uncovered simulations was reached in the beginning of the indentor penetration, whereas in the covered simulations it was reached later. This phenomenon is likely related to the differences in the evolution of the deformation patterns between different experiment types (see Section 4.2.3).

The friction at the long walls somewhat increased the measured maximum rubble load F_R^m. This can be seen from the values of F_μ at the instant of the maximum rubble load F_R^m given in Fig. 17a and b. As the figure shows, F_μ values increased with h. This is due to the

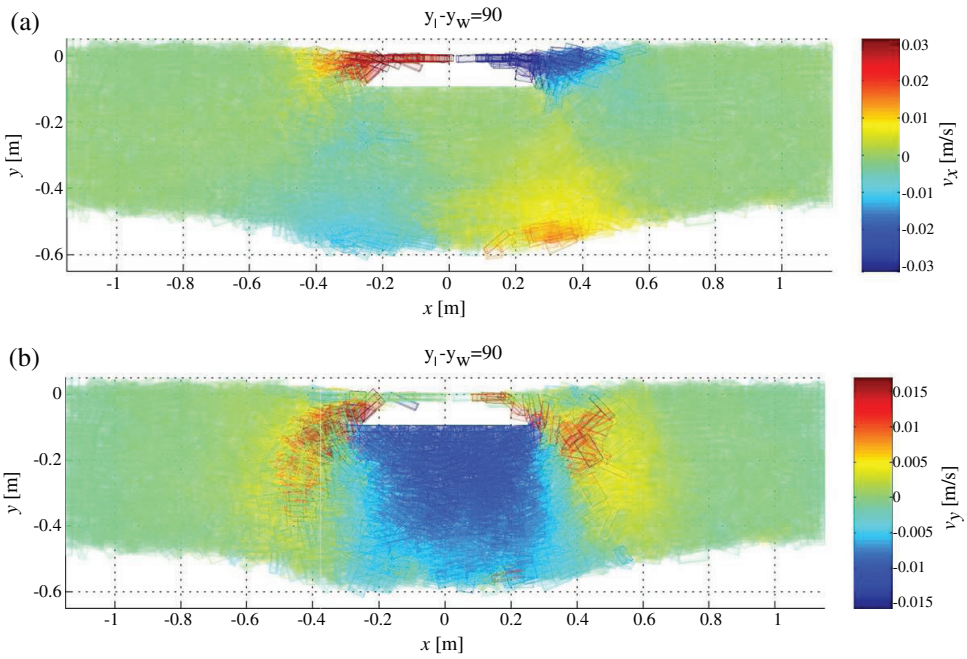

Fig. 10. Components (a) v_x and (b) v_y of block centroid velocities in a simulated uncovered punch through experiment towards the end of the indentor stroke. Rubble moving on top of the indentor in (a) enables the upward movement of rubble in (b). In the simulation, rubble thickness was 0.5 m, basin width 2.3 m and the indentor velocity 10 mm/s.

increase in the number of frictional contacts between rubble mass and the walls with h. The data in the figure together with the maximum rubble load F_R^m values in Fig. 6 was used to estimate the total contribution of F_μ^m on F_R^m: sum of F_μ^m on opposing long walls accounted for 2 (with $h=0.3$ m) to 6 ($h=0.5$ m) % of F_R^m in uncovered and for 3 ($h=0.3$ m) to 8 ($h=0.5$ m) % of F_R^m in covered basin simulations.

As Fig. 17 further shows, the values of F_μ at short walls were low in all simulations and virtually vanished in covered simulations due to the covers restricting the upward movement of the rubble. Low F_μ values in Fig. 17 indicate, that the rubble in the vicinity of the walls did not move. This is in accordance with the observations during the experiments and was also shown by the deformation patterns in Section 4.2. In addition and more importantly, the low F_μ values on short walls together with approximately equal F_μ values on long walls with both w_b indicate, that the rubble deformation patterns were not affected by the basin width in the experiments.

5.2. Derivation of material parameters

The results presented in the previous section can be used to discuss the derivation of the material parameters from the experimental results. For this, the Mohr–Coulomb material model commonly used in interpretation of punch through experiment results is considered. In the model, the shear strength τ is given by

$$\tau = c + \sigma \tan\phi, \tag{2}$$

where σ is the confining pressure and material parameters c and ϕ are the cohesion and Mohr–Coulomb friction angle of the material, respectively.

An estimate for the experimental τ can be derived from the results using a formula similar to that in Azarnejad and Brown (2001). In the estimate, the maximum rubble load F_R^m is assumed to include components due to rubble buoyancy (F_B), friction due to basin walls (F_μ) and shearing of the rubble (F_τ), hence $F_R^m = F_\tau + F_B + F_\mu$. Further it is assumed that the rubble fails on two distinct failure planes leading to $F_\tau = 2\tau bh$, where b is the basin width and h the rubble depth. With these assumptions, the rubble shear strength can be derived from

$$\tau = \frac{F_\tau}{2bh} = \frac{F_R^m - F_B - F_\mu}{2bh}. \tag{3}$$

Here, the shear strength values for the rubble were estimated by using a common first approximation of indentor supporting only the rubble mass directly under it at the instant of F_R^m. In this case, the buoyant component in previous equation can be approximated from $F_B \approx (1-\eta)(\rho_w - \rho_b) w_I bhg$, where w_I is the indentor width. The τ values derived from the previous equation using this value of F_B are shown in Fig. 18 for the simulations and experiments. The τ values from covered experiments and all simulations in the figure clearly suggest, that τ increased with h. The τ values given in the figure are fairly close to those measured for unconsolidated ice rubble in similar experiments by (Azarnejad and Brown, 2001). It should also be noticed, that if the friction on the long walls is not taken account, Eq. (3) yields τ values up to 10% higher than given in the figure.

The effect of increasing confining pressure on the derivation of the Mohr–Coulomb friction angle ϕ of the rubble can be studied using the equations above. For this, Eq. (2) is substituted into Eq. (3) and $c=0$ is assumed, leading to following dependency between σ and F_τ:

$$\sigma \tan\phi = \frac{F_\tau}{2bh}. \tag{4}$$

The results in Section 4.3.1 indicate, that σ increases during the indentor penetration: the lateral force F_x was observed to increase up to roughly 50% from its initial value. Therefore, even if a

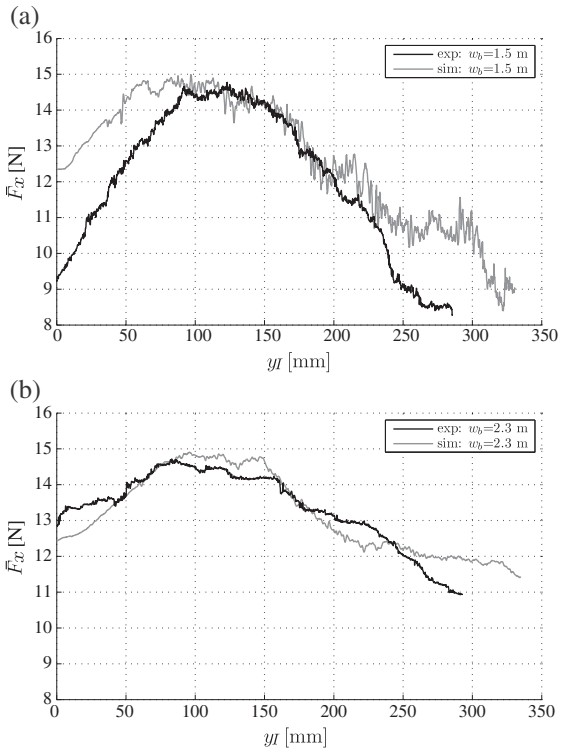

Fig. 11. Mean lateral force $\bar{F}_x$ records from covered basin experiments with both basin widths w_b. In the experiments and simulations shown, rubble thickness h was 0.5 m. The indentor velocity v_I in the experiments was 2.5 mm/s and 10 mm/s in the simulations.

reasonable estimate for the initial value of σ was available, e.g. derived from the initial hydrostatic pressure within the rubble, it is not necessarily an accurate estimation for σ during an experiment. If this estimate was anyhow used to solve ϕ for the rubble from Eq. (2), ϕ could become overestimated as demonstrated in the following using a simplified example.

Assuming, that a value for shear strength τ has been derived from the experimental results (see e.g. Azarnejad and Brown (2001) for derivation of τ) and $c=0$ in Eq. (2), the ϕ value for some ratio σ/τ is given by $\phi=\arctan(\tau/\sigma)$. First, let $\phi_0=\arctan(\tau/\sigma_0)$, where σ_0 is the initial confining pressure within the pile, and $\phi_a=\arctan(\tau/\sigma_a)$, where σ_a is the actual confining pressure. Then, the change in the estimate of ϕ due to change in σ can be studied using ratio ϕ_0/ϕ_a.

Fig. 19 shows the values of ϕ_0/ϕ_a for different ratios of σ_a/σ_0 as function of σ_0/τ. As the figure shows, with low σ_0/τ ratios the values of ϕ are likely estimated well. On the other hand, large σ_0/τ ratios lead to an overestimation of ϕ if actual σ value is underestimated. The 50% increase in σ ($\sigma_a/\sigma_0=1.5$), suggested by the increase in F_x (see Section 1),would lead to clear overestimation of ϕ even with moderate σ_0/τ ratios. It should be noticed, that $\sigma_0/\tau=1$ would lead to $\phi=45°$ (ϕ decreases with increase in σ_0/τ), which is already in the high end of values suggested for ice rubble (Ettema and Urroz, 1989; Liferov and Bonnemaire, 2005).

Hence, an overestimation of ϕ can occur due to increasing σ and the derivation of ϕ from the results is thus challenging. Further, the use of Mohr–Coulomb model is difficult as even σ_0 is not constant through the rubble thickness (Ettema and Schaefer, 1986). It should also be noticed, that if the assumption $c=0$ for the rubble was incorrect even further overestimation of ϕ would result (Liferov and Bonnemaire, 2005). Further, the control on c in experiments is difficult as the freeze bonds between the ice blocks start to form within very short time periods (Ettema and Schaefer, 1986; Repetto-Llamazares et al., 2011). Due to these reasons, some other experimental technique should be utilized to measure ϕ for the rubble, as also suggested by Serré (2011).

5.3. Boundary conditions and material modelling

The results in Sections 2.3 and 4.1 demonstrate, that the occurrence of the measured maximum load does not necessarily correspond to the occurrence of maximum load due to rubble. Still, the maximum measured load is usually first of interest when material properties of the rubble are derived from the results of a punch through test. For this derivation of the material properties, the measured load has to be divided into components due to rubble resistance and due to other sources, e.g. hydrodynamics and experimental equipment buoyancy.

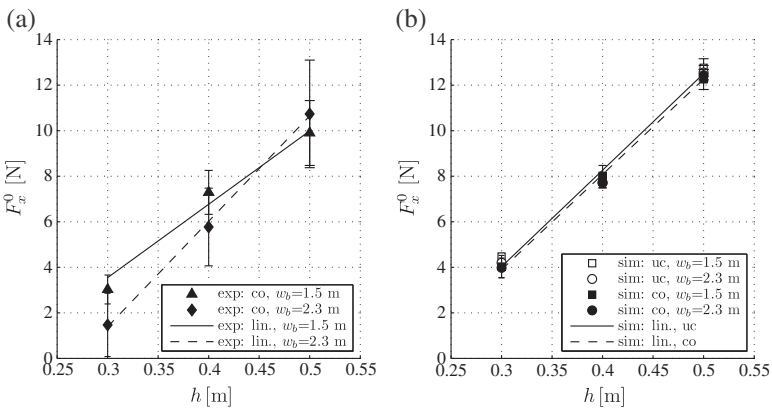

Fig. 12. Mean values of initial lateral force F_x^0 with their standard deviations for all rubble thicknesses h used and both basin widths w_b in (a) covered basin experiments and in (b) simulations of uncovered (un) and covered (co) basin experiments. In (a), F_x^0 values from the experiments with $v=2.5$ mm/s and 5 mm/s and in (b) simulations with $v_I=10$ mm/s were included. In addition in (a), linear fits for both basin widths w_b are shown. The fits in (b) are for simulations of uncovered and covered basin experiments with both w_b included.

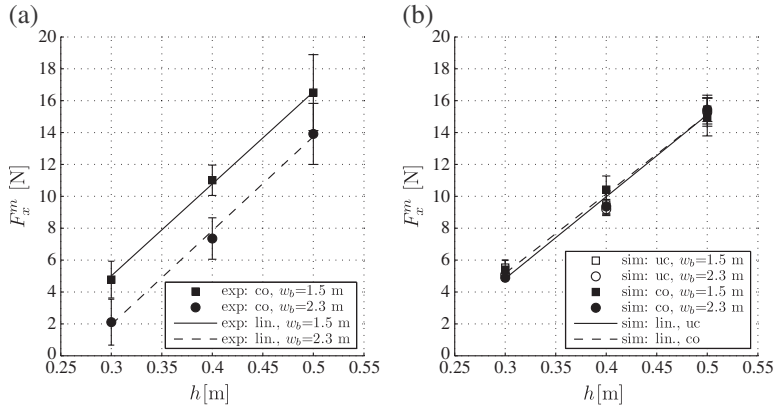

Fig. 13. Mean values of maximum lateral force F_x^m with their standard deviations for all rubble thicknesses h used and both basin widths w_b in (a) covered (co) basin experiments and in (b) simulations of uncovered (un) and covered (co) basin experiments. In (a), F_x^m values from the experiments with $v = 2.5$ mm/s and 5 mm/s and in (b) simulations with $v_I = 10$ mm/s were included. In addition, linear fits for both w_b in (a) are shown. In (b), linear fits for different boundary conditions are given, as both w_b yielded to approximately equal value of F_R^m.

As presented in Section 4, maximum rubble load F_R^m was in general reached with higher indentor displacement in the covered basin than in the uncovered basin experiments. This difference between test types was related to the evolution of the displacing rubble mass (see Figs. 8 and 9). The maximum measured indentor load occurred instead immediately after the indentor submergence and was related to hydrodynamic force acting on the indentor platen (Polojärvi and Tuhkuri, 2012) i.e. the displacement at maximum measured load was related to the experimental set up rather than rubble load.

In the aspect of material parameters in e.g. Mohr–Coulomb model (Eq. (2)), the division of the measured load into components due to cohesion, rubble buoyancy and frictional resistance is important. Out of these, the buoyant and frictional components are changed by the evolution of the deformation patterns and the change in confining force (Sections 4.2.3 and 4.3.1). In addition, the change in the boundary conditions makes the division even more complicated: the results are not only altered by rubble properties, but also by the boundary conditions of the experiment (see Figs. 8 and 9).

6. Conclusions

Laboratory scale punch through tests on floating rubble consisting of plastic blocks were conducted and simulated with a 3D discrete numerical model. The purpose was to analyse the experimental method and to validate the model. The motivation of using plastic blocks instead of ice was to simplify the interpretation of results as the plastic blocks do not freeze together. The results from the simulations were found to be in agreement with the experimental results. The main results presented in this paper are:

- The ability of the discrete numerical method to simulate laboratory scale punch through experiments on unconsolidated rubble was demonstrated: the experimental force records and the deformation patterns of the rubble during indentor stroke were in good agreement with the simulation results.
- The evolution of the deformation patterns was shown to be closely related to the load due to the rubble material. This relation was

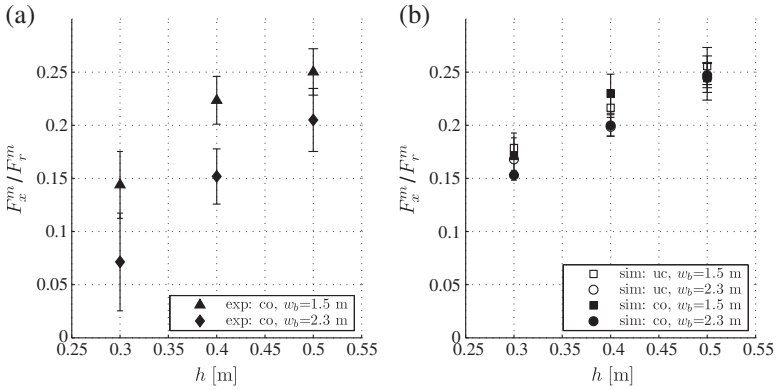

Fig. 14. Mean values of ratio F_x^m/F_R^m with their standard deviations of maximum lateral force F_x^m to maximum rubble load F_R^m for all rubble thickness h and both basin widths w_b in (a) covered (co) basin experiments and in (b) simulations of uncovered (un) and covered (co) basin experiments. The data used in the figures is given in Figs. 6 and 13.

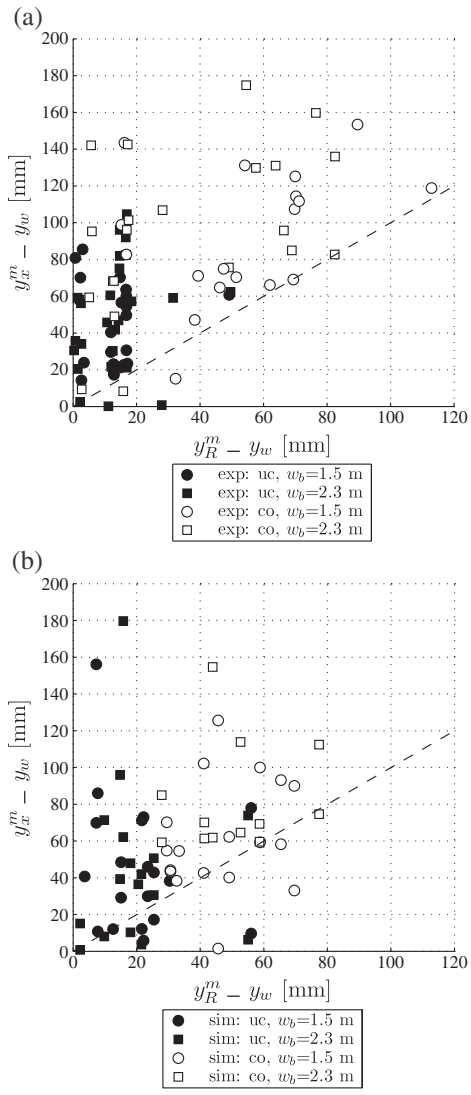

Fig. 15. Indentor distance from water surface y_w at maximum lateral load y_x^m against the distance at maximum rubble load y_R^m: (a) uncovered (un) and covered (co) experiments and (b) corresponding simulations. In (a), experiments with indentor velocities $v_I = 2.5$ mm/s and $v_I = 5$ mm/s are included. Data from simulations in (b) is from simulations with $v_I = 10$ mm/s. Figures include data from experiments and simulations with both basin widths w_b and all rubble thicknesses h. In addition in both figures, the case of $y_x^m = y_R^m$ is shown with dashed line.

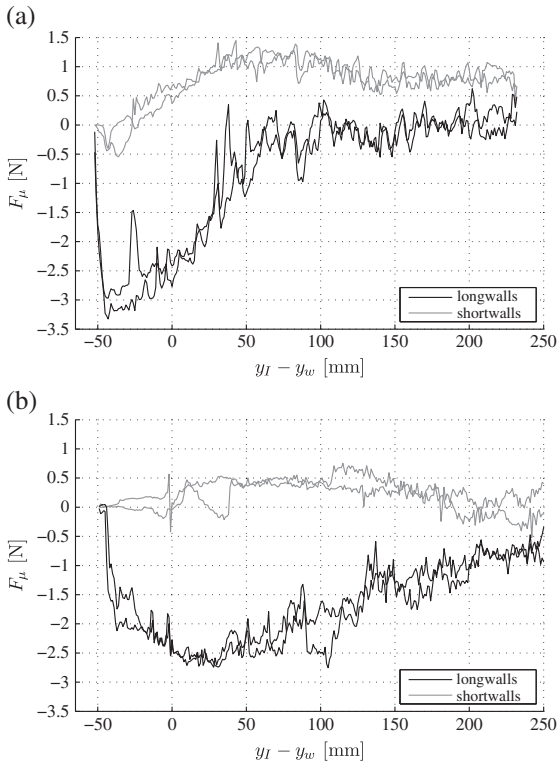

Fig. 16. Typical records of frictional force F_μ applied by the basin walls onto the rubble in (a) uncovered and (b) covered basin simulations. Negative (positive) F_μ values indicate the friction at a wall resisting downwards (upwards) rubble movement. Long and short walls in the legend refer to the opposing walls at $z = \pm 0.25$ m and $x = \pm w_b/2$, respectively (see Fig. 1). The data is from a simulation with basin width $w_b = 1.5$ m and rubble thickness $h = 0.5$ m.

shown to effect the load curve during the whole indentor stroke. This demonstrates the importance of the numerical model to correctly represent the rubble deformation and its mass flow in simulations.

- The lateral force and thus the confining pressure were in general still increasing when the maximum rubble load was reached. This could lead to an overestimation of the friction angle of the rubble if the increase in confining pressure is not properly taken into account when interpreting the results.
- The maximum load due to rubble material does not necessarily occur simultaneously with the measured maximum load in the punch through experiments: first was closely related to the rubble deformation whereas the latter was related to the hydrodynamics. Due to this the interpretation of the experimental records in the aspect of material modelling could be challenging, if the deformation pattern of the rubble is not known accurately.

Acknowledgements

The experiments and the development of the numerical model were performed by AP, and the analysis of the results by AP and JT. The motion tracking application used in the visual analysis of the experiments was developed by OK. The financial support for the work of AP by the Ministry of Education of Finland through the National Graduate School in Engineering Mechanics and from the Graduate Program of Aalto University, School of Engineering, is gratefully acknowledged.

Appendix A. Mechanics

In the discrete numerical model for the rubble used here, the pile consisted of individual rigid blocks which interacted through contacts. Due to the relatively low force levels in the experiments, the effect of deformation of individual blocks on results was likely negligible and the assumption of rigid blocks thus applicable. The forces and moments

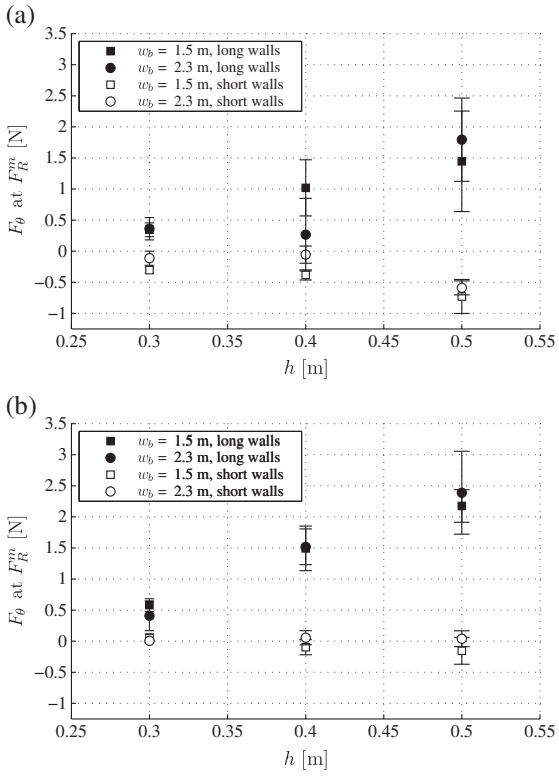

Fig. 17. Frictional force F_μ as maximum rubble load F_R^m is reached in (a) uncovered and (b) covered simulations. Negative (positive) F_μ indicates a wall resisting downwards (upwards) rubble movement. Long and short walls in the legend refer to the opposing walls at $z=\pm 0.25$ m and $x=\pm w_b/2$ m, respectively (see Fig. 1).

acting on the simulated blocks were due to contacts, buoyancy, gravitation, and water drag. The determination of these forces is presented below. The moments can be derived from the equations below.

Contact forces between the blocks were derived using penalty function and potential contact force method described in detail in Munjiza and Andrews (2000) and Munjiza (2004). The blocks were

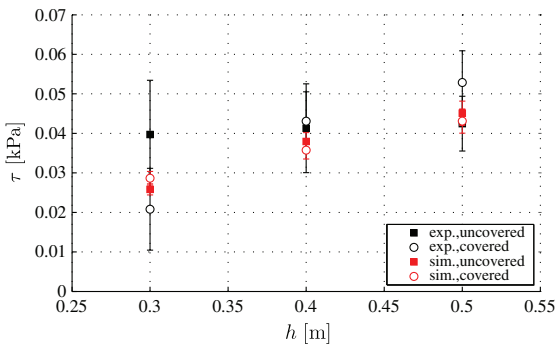

Fig. 18. Mean values of rubble shear strength τ with its standard deviations derived using Eq. (3) for all rubble thicknesses h. The data from experiments (exp.) and simulations (sim.) with both basin widths w_b is included in the data shown in the figure.

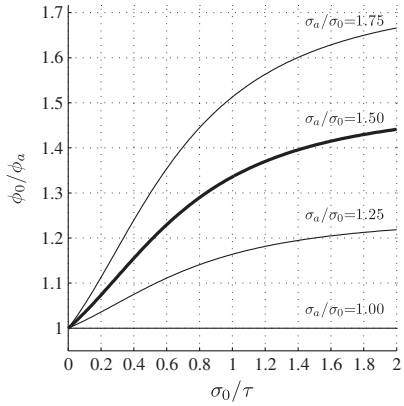

Fig. 19. The overestimation of friction angle ϕ from Eq. (2) with zero cohesion ($c=0$). In the figure ϕ_0 is the friction angle yielded by the results and initial confining pressure σ_0 within the rubble. Further, ϕ_a and σ_a are the actual friction angle and confining stress, respectively. Shear stress τ is assumed to have been derived from the experiments. The lateral load records (Section 4.3.1) suggested values up to $\sigma_a/\sigma_0 \approx 1.5$ shown with bold black line.

here meshed into tetrahedrons and contact forces were solved for tetrahedrons. The total contact force acting on a block was then achieved by superposition of the forces acting on its tetrahedrons.

In the potential contact force method, a potential φ with continuous first partial derivatives with respect to spatial coordinates is defined in every point P of each finite element volume Ω. Further, $\varphi=\varphi(P)$ vanishes on finite element boundaries Γ for smooth collision response. Hence

$$\varphi(P) > 0, \quad P \in \Omega \wedge \varphi(P) = 0, \quad P \in \Gamma. \tag{A.1}$$

As the blocks here were each divided into tetrahedrons, the volume coordinates of these tetrahedrons were used as function for $\varphi(P)$ (Munjiza, 2004).

The contact force $d\mathbf{f}_\varphi$ applied to an infinitesimal volume element $d\Omega_o$ penetrating into φ is determined from the gradient of φ as (Fig. A.1 a)

$$\frac{d\mathbf{f}_\varphi(P)}{d\Omega_o} = -s\nabla\varphi(P), \tag{A.2}$$

where s is a positive constant penalty term. The contact force $\mathbf{f}_\varphi$ due to $\varphi(P)$ was determined by integration over the overlap volume Ω_o of two colliding elements from

$$\mathbf{f}_\varphi = -s\int_{\Omega_o}\nabla\varphi(P)\,d\Omega = -s\int_{\Gamma_o}\varphi(P)\mathbf{n}\,d\Gamma, \tag{A.3}$$

where Gauss's theorem is used and $\mathbf{n}$ is the unit outer normal of Γ_o (Fig. A.1 b). The distributed load due to φ is thus reduced to a force acting on a single point on Γ_o which is solved and used as a point of contact.

The inelasticity in collisions is modelled by using viscous damping relative to the rate of change in overlap volume. The viscous component of the normal force $\mathbf{f}_v$ is defined as

$$\mathbf{f}_v = c\Gamma_0(\mathbf{v}_r\cdot\mathbf{n})\mathbf{n}, \tag{A.4}$$

where $\mathbf{v}_r\cdot\mathbf{n}$ is the normal component of the relative velocity of the contacting blocks at the point of application of $\mathbf{f}_\varphi$ and c is the viscous damping constant.

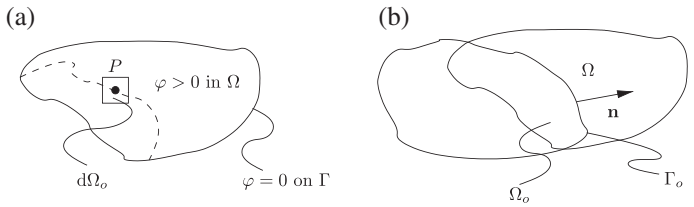

Fig. A.1. (a) An infinitesimal volume element $d\Omega_o$ at point P penetrating into a finite element with volume Ω and (b) the overlap volume Ω_o of two elements.

No tensile forces between colliding blocks are allowed and thus the total contact force $\mathbf{f}_c$ should always acts on the direction of $-\mathbf{n}$ in contacts. Hence the following condition was used:

$$\mathbf{f}_c = \begin{cases} 0, & \text{if } |\mathbf{f}_\varphi| - |\mathbf{f}_v| < 0 \\ \mathbf{f}_\varphi - \mathbf{f}_v & \text{else.} \end{cases} \tag{A.5}$$

Sliding friction was modelled by using dynamic Coulomb friction model. Frictional force $\mathbf{f}_\mu$ was solved from

$$\mathbf{f}_\mu = -\mu|\mathbf{f}_c|\frac{\mathbf{v}_r - \mathbf{v}_r\cdot\mathbf{n}}{|\mathbf{v}_r - \mathbf{v}_r\cdot\mathbf{n}|}, \tag{A.6}$$

where μ is the friction coefficient and $\mathbf{v}_r - \mathbf{v}_r\cdot\mathbf{n}$ is the tangential component of the relative velocity of contacting blocks at the point of contact.

The determination of the buoyant force due to the water and gravitational force acting on the blocks in the simulations was fairly straightforward. For a partially submerged block shown in Fig. A.2, the buoyant force was determined by integrating hydrostatic pressure over the submerged part A_s of the block surface A. For a block with its total volume submerged or above the water level, buoyant force was applied on block centroid. The gravitational force was always applied on the block centroid as further shown in Fig. A.2.

The external force $\mathbf{f}_e$, due to buoyancy and gravitation, for a block was determined from the following equation defined in three parts according to the block position (see Fig. A.2 for directions):

$$\mathbf{f}_e = \begin{cases} \rho_b V g\mathbf{j}, & \text{if above water level.} \\ \rho_w g\int_{A_s}(y - y_w)(-\mathbf{n}_b\cdot\mathbf{j})dA\mathbf{j} + \rho_b V g\mathbf{j}, & \text{if partially submerged.} \\ (\rho_b - \rho_w)V g\mathbf{j}, & \text{if submerged.} \end{cases} \tag{A.7}$$

In the previous equation V is the volume of the block, ρ_b and ρ_w are the material densities of the blocks and water, respectively, g is the gravitational acceleration, y_w the water line, $\mathbf{n}_b$ the block surface unit normal and $\mathbf{j}$ is a unit vector parallel to global y-axis.

Rigorous modelling of the hydrodynamics in the experiments would be challenging and was not attempted here. Instead, only a simplified model for the water drag acting on the blocks was implemented and used in the simulations. The model was derived

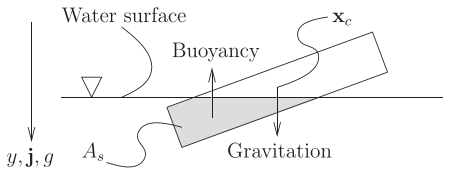

Fig. A.2. The gravitational and buoyant force acting on a partially submerged block. Whereas the gravitational force is always constant and applied on block centroid $\mathbf{x}_c$, the buoyant force is dependent on submerged part of the block. Submerged part of the block surface A_s is shown in gray. The figure also shows the directions of gravitational acceleration g and unit vector $\mathbf{j}$ both aligning with global y-axis.

to approximate the pressure drag on the blocks. The pressure drag is commonly solved from (Granger, 1995)

$$D = C_d\left(\frac{1}{2}\rho_w U^2 A_p\right), \tag{A.8}$$

where C_d is the drag coefficient, U the velocity and A_p the projected area (area projected into the direction of U) of a block. The direction of D in the previous equation is opposite to U.

For the approximation of D in Eq. (A.8), the drag force was modelled as a distributed load acting on part of the submerged block surface A_s with surface velocity $\mathbf{u}_A$ having $\mathbf{u}_A\cdot\mathbf{n}_b > 0$ i.e. on the part of A_s with $\mathbf{u}_A$ having a positive normal component. Total drag force $\mathbf{f}_d$ acting on the block was then achieved from the integral

$$\mathbf{f}_d = \begin{cases} -\frac{1}{2}C_d\rho_w\int_{A_s}(\mathbf{u}_A\cdot\mathbf{n}_b)^2\mathbf{n}_b\, dA, & \text{if } \mathbf{u}_A\cdot\mathbf{n}_b > 0 \\ 0 & \text{otherwise.} \end{cases} \tag{A.9}$$

In the case of pure translation of the block ($\mathbf{u}_A = const.$on the part of A_s into the direction $\mathbf{u}_A$), the previous equation yields to $\mathbf{f}_d$ with absolute value equal to D in Eq. (A.8).

Appendix B. Effect of loading rate

The simulations presented in the paper were run with indentor velocity $v_I = 10$ mm/s, whereas in the experiments the indentor velocities $v_I = 2.5$ mm/s and $v_I = 5$ mm/s were used. For reference, simulations with $v_I = 5$ mm/s were runwith negligible change in results. This is shown by mean rubble load records $\bar{F}_R$ from simulations with $v_I = 10$ mm/s and 5 mm/s in Fig. B.1. The figure clearly shows, that the $\bar{F}_R$ records with these indentor velocities yielded virtually equal $\bar{F}_R$ records.

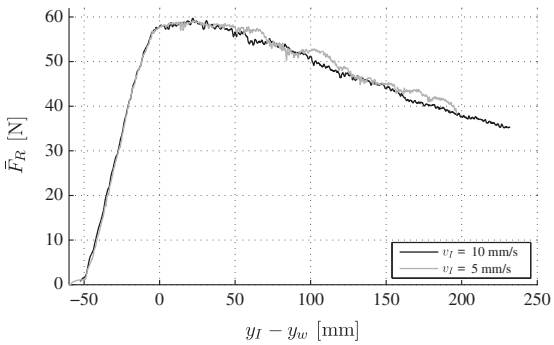

Fig. B.1. Mean rubble load $\bar{F}_R$ records from the simulations with indentor velocities $v_I = 5$, 10 and 40 mm/s of (a) uncovered and (b) covered experiments. The data is from simulations with rubble thickness $h = 0.5$ m and basin width $w_b = 1.5$ m.

References

Azarnejad, A., Brown, T., 2001. Small-scale plane strain punch tests. Journal of Cold Regions Engineering 15 (3), 135–153 (September).

Azarnejad, A., Frederking, R., Brown, T., 1999. Ice rubble strength from small scale punch through tests. Proceedings of OMAE99, 19th International Conference on Offshore Mechanics and Arctic Engineering, pp. 1–9.

Bruneau, S., Crocker, G., McKenna, R., Croasdale, K., Metge, M., Ritch, R., Weaver, J., 1998. Development of techniques for measuring in situ ice rubble shear strength. Ice in Surface Waters, Proc. of the 14th International Symposium on Ice, IAHR, vol. 2, pp. 1001–1007 (Potsdam, New York, USA).

Croasdale, K.R., Bruneau, S., Christian, D., Crocker, G., English, J., Metge, M., Ritch, R., 2001. In-situ measurements of the strength of first-year ice ridge keels. Proceedings of the 16th International Conference on Port and Ocean Engineering under Arctic Conditions, POAC'01, vol. 3, pp. 1445–1454 (Ottawa, Ontario, Canada).

Cundall, P., Strack, O., 1979. A discrete numerical model for granular assemblies. Géotechnique 29, 47–65.

Ettema, R., Schaefer, J.A., 1986. Experiments on freeze-bonding between ice blocks in floating ice rubble. Journal of Glaciology 32 (112), 397–403.

Ettema, R., Urroz, G.E., 1989. On internal friction and cohesion in unconsolidated ice rubble. Cold Regions Science and Technology 16 (3), 237–247.

Granger, R.A., 1995. Fluid Mechanics. Dover Publications, N.Y, USA.

Haase, A., Polojärvi, A., Tuhkuri, J., 2010. 3D discrete numerical modelling of conical structure–ice rubble interaction. Proceedings of 20th IAHR International Symposium on Ice. IAHR, Lahti, Finland (electronic publication).

Heinonen, J., 2004. Constitutive modeling of ice rubble in first-year ridge keel. Doctoral Thesis, TKK, VTT Publications 536. Espoo, Finland, 2004, 142 pp, ISSN 1235–0621.

Heinonen, J., Määttänen, M., 2000. Ridge loading experiments, field experiments in winter 2000. LOLEIF Progress Report No. 10. TKK (40 pp.).

Heinonen, J., Määttänen, M., 2001a. Full-scale testing of ridge keel mechanical properties in LOLEIF project (August 12–17) Proceedings of the 16th International Conference on Port and Ocean Engineering under Arctic Conditions, POAC'01, vol. 3, pp. 1435–1444 (Ottawa, Ontario, Canada).

Heinonen, J., Määttänen, M., 2001b. Ridge keel mechanical properties — testing. Field experiments in winter 2001. ReportSTRICE. TKK (39 pp.).

Hopkins, M., 1992. Numerical simulation of systems of multitudinous polygonal blocks. Tech. Rep. 92-22. Cold Regions Research and Engineering Laboratory, CRREL (69 pp.).

Hopkins, M., 1998. Four stages of pressure ridging. Journal of Geophysical Research 103 (C10), 21,883–21,891.

Hopkins, M., Tuhkuri, J., Lensu, M., 1999. Rafting and ridging of thin ice sheets. Journal of Geophysical Research 104 (C6), 13605–13613.

Jensen, A., Løset, S., Høyland, K.V., Liferov, P., Heinonen, J., Evers, K.-U., Määttänen, M., 2001. Physical modelling of first-year ice ridges — part II: mechanical properties. Proceedings of the 16th International Conference on Port and Ocean Engineering under Arctic Conditions, POAC'01, vol. 3, pp. 1493–1502 (Ottawa, Ontario, Canada).

Kuroiwa, D., 1961. A study of ice sintering. Tellus 13 (2), 252–259.

Lemee, E., Brown, T., 2002. Small-scale plane strain punch tests. Ice in the Environment: Proceedings of the 16th IAHR International Symposium on Ice.

Leppäranta, M., Hakala, R., 1992. The structure and strength of first-year ice ridges in the Baltic Sea. Cold Regions Science and Technology 20 (3), 295–311.

Liferov, P., 2005. Ice rubble behaviour and strength: part II. Modelling. Cold Regions Science and Technology 41 (2), 153–163.

Liferov, P., Bonnemaire, B., 2005. Ice rubble behaviour and strength: part I. Review of testing and interpretation of results. Cold Regions Science and Technology 41, 135–151.

Liferov, P., Jensen, A., Høyland, K., 2002. On analysis of punch tests on ice rubble. Proceedings of the 16th International Symposium on Ice, vol. 2, pp. 101–110 (Dunedin, New Zealand).

Liferov, P., Jensen, A., Høyland, K., 2003. 3D finite element analysis of laboratory punch tests on ice rubble. Proceedings of the 17th International Conference on Port and Ocean Engineering under Arctic Conditions, POAC'03, vol. 2, pp. 611–621 (Trondheim, Norway).

MATLAB, 2009. Version 7.9.0 (R2009b). The MathWorks Inc., Natick, Massachusetts.

Munjiza, A., 2004. The Combined Finite–Discrete Element Method. John Wiley & Sons Ltd., Chichester, England.

Munjiza, A., Andrews, K., 2000. Penalty function method for combined finite-discrete element systems comprising large number of separate bodies. 49 (11), 1377–1396.

Munjiza, A., Owen, D., Bićanić, N., 1995. A combined finite-discrete element method in transient dynamics of fracturing solids. 12, 145–174.

Paavilainen, J., Tuhkuri, J., 2012. Parameter effects on simulated ice rubbling forces on a wide sloping structure. Cold Regions Science and Technology, http://dx.doi.org/10.1016/j.coldregions.2012.04.005.

Paavilainen, J., Tuhkuri, J., Polojärvi, A., 2006. Discrete element simulation of ice pile-up against an inclined structure. Proceedings of the 18th International Symposium on Ice, IAHR, vol. 2, pp. 177–184 (Sapporo, Japan).

Paavilainen, J., Tuhkuri, J., Polojärvi, A., 2009. 2D combined finite–discrete element method to model multi-fracture of beam structures. Engineering Computations 26 (6), 578–598.

Paavilainen, J., Tuhkuri, J., Polojärvi, A., 2011. 2D numerical simulations of ice rubble formation process against an inclined structure. Cold Regions Science and Technology 68 (1–2), 20–34.

Polojärvi, A., Tuhkuri, J., 2009. 3D discrete numerical modelling of ridge keel punch through tests. Cold Regions Science and Technology 56 (1), 18–29.

Polojärvi, A., Tuhkuri, J., 2010. Modelling ridge keel freeze bonds in finite–discrete element method simulations. Proceedings of 20th IAHR International Symposium on Ice. IAHR, Lahti, Finland (electronic publication).

Polojärvi, A., Tuhkuri, J., 2012. Velocity effects in laboratory scale punch through experiments. Cold Regions Science and Technology 70 (1), 81–93.

Repetto-Llamazares, A., Høyland, K., Evers, K.-U., 2011. Experimental studies on shear failure of freeze-bonds in saline ice: part I. Set-up, failure mode and freeze-bond strength. Cold Regions Science and Technology 65 (3), 286–297.

Serré, N., 2011. Mechanical properties of model ice ridge keels. Cold Regions Science and Technology 67 (3), 89–106.

Tuhkuri, J., Polojärvi, A., 2005. Effect of particle shape in 2D ridge keel deformation simulations. Proceedings of the 18th International Conference on Port and Ocean Engineering under Arctic Conditions, POAC'05, vol. 2, pp. 939–948 (Potsdam, New York, USA).